ADVANCED ENERGY MATERIALS
www.advenergymat.de

# PFAS Free Organic Carbonate-Based Electrolyte Formulation for LNMO||SiGr Cell Chemistry

*Maike Leopold, Constantin Lürenbaum, Tobias Brake, Christian Wölke, Peng Yan, Martin Winter, Sascha Nowak, Simon Wiemers-Meyer, and Isidora Cekic-Laskovic**

**A per- and polyfluoroalkyl substances (PFAS) free electrolyte formulation for the high voltage lithium nickel manganese oxide (LNMO)||silicon-graphite (SiGr) per- and polyfluoroalkyl substances (20 wt.% silicon) cell chemistry is developed. The high upper cut-off voltage of 4.9 V, together with the substantial volume expansion of the silicon-graphite negative electrode, imposes stringent demands on the electrochemical stability of the electrolyte. A newly developed PFAS free electrolyte formulation incorporating lithium difluoro(oxalato)borate (LiDFOB) alongside cost-effective organic carbonate solvents ethylene carbonate (EC) and ethyl methyl carbonate (EMC) enables stable operation of LNMO||SiGr cell chemistry. Improved galvanostatic cycle life from 145 cycles to 245 cycles (69 %) can be achieved in the presence of 4 wt.% LiDFOB. LiDFOB effectively suppresses the transesterification often observed in organic carbonate-based electrolytes by scavenging lithium alkoxides and leads to a reduction of transition metal (TM) dissolution. These properties contribute to the formation of an effective solid electrolyte interphase (SEI) and cathode electrolyte interphase (CEI), resulting in improved galvanostatic cycling stability and overall electrochemical performance. The developed PFAS free electrolyte formulation constitutes a promising pathway for high-voltage lithium ion cells, combining environmental safety with high electrochemical performance.**

## 1. Introduction

Lithium ion batteries (LIB) are widely used in electric vehicles and have undergone continuous advancements to meet the growing demand for higher energy densities.[1,2] This can potentially be achieved by using a silicon-containing negative electrode and the high-voltage lithium nickel manganese oxide ($LiNi_{0.5}Mn_{1.5}O_4$) positive electrode.[3–5] Compared to graphite, silicon-containing negative electrodes are characterized by their high specific capacity of 3590 mAh $g^{-1}$ for $Li_{3.75}Si$ (graphite: 372 mAh $g^{-1}$). In the Earth's crust, silicon is the second most abundant element.[6–11] However, using silicon results in considerable volume expansion of ≈300 % during full lithiation, and the resulting electrode has a higher working potential of ≈0.4 V vs $Li|Li^+$ as compared to graphite with ≈0.1 V vs $Li|Li^+$.[10,12] High volume expansion results in particle cracking, leading to an ineffective solid electrolyte interphase (SEI), irreversible loss of capacity in the first cycle, and mechanical fracture. These issues result in rapid capacity fading during galvanostatic cycling.[10,11,13] To minimize these challenges, silicon is combined with graphite (SiGr), enabling the advantages of both materials to be utilized, particularly in terms of volume expansion and theoretical capacity.[12,14,15] In addition to the attempts to increase the specific capacity in the participating electrodes of an LIB, an alternative approach to enhance the energy density by increasing the operation voltage, which is why LNMO is selected as the positive electrode material. LNMO has a theoretical specific capacity of 147 mAh $g^{-1}$ and an operation potential of 4.7 V vs $Li|Li^+$,[16–19] which leads to a higher energy density of 650 Wh $kg^{-1}$ on electrode level compared to lithium iron phosphate ($LiFePO_4$) (510 Wh $kg^{-1}$) counterpart but which is lower than that of Lithium nickel manganese cobalt oxide ($LiNi_{0.8}Co_{0.1}Mn_{0.1}O_2$) (780 Wh $kg^{-1}$).[20–22] Cost volatility and environmental impact are further important considerations, where the absence of cobalt and comparatively low nickel content are benefits of the LNMO electrode.[23,24] However, LNMO-based cells often suffer from rapid capacity fading due to strong oxidative electrolyte decomposition and transition metal (TM) dissolution.[22,25–28] To improve the cycling stability of LNMO||SiGr cells, an appropriate electrolyte that can form an effective SEI and cathode electrolyte interphase (CEI) in the high-voltage area up to 4.9 V is to be

M. Leopold, C. Wölke, P. Yan, M. Winter, I. Cekic-Laskovic
Helmholtz-Institute Münster (IMD-4)
Forschungszentrum Jülich GmbH
Corrensstraße 48, 48149 Münster, Germany
E-mail: i.cekic-laskovic@fz-juelich.de

C. Lürenbaum, T. Brake, M. Winter, S. Nowak, S. Wiemers-Meyer
MEET Battery Research Center
University of Münster
Corrensstraße 46, 48149 Münster, Germany

The ORCID identification number(s) for the author(s) of this article can be found under https://doi.org/10.1002/aenm.202505133



**DOI: 10.1002/aenm.202505133**

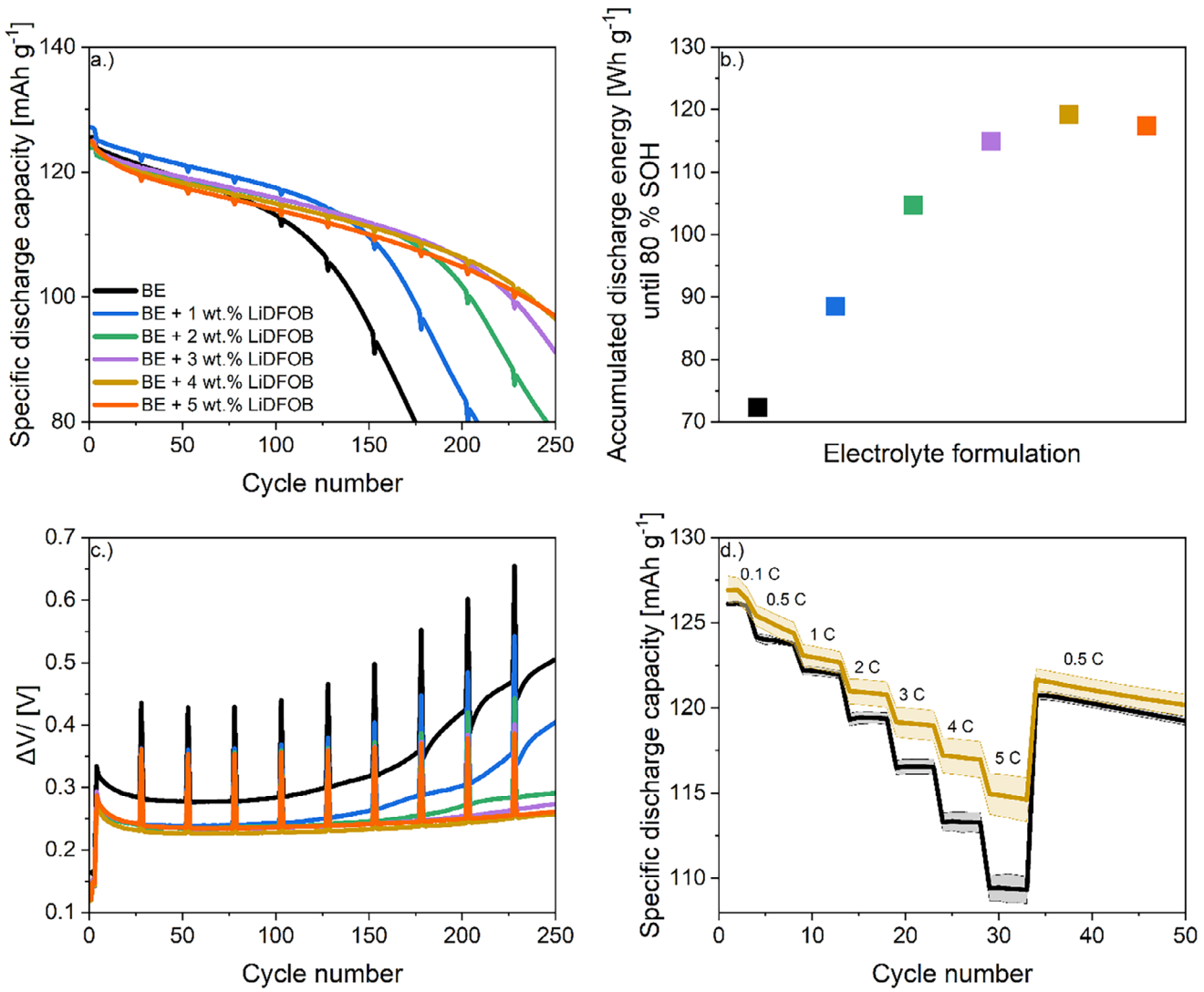


**Figure 1.** Mean specific discharge capacity vs cycle number a), accumulated discharge energy until 80 % SOH vs electrolyte formulation b), Δ*V* vs cycle number c) of the BE electrolyte and BE + 1–5 wt.% LiDFOB. Rate capability experiment with various C-rates between 0.1 and 5 C of the BE electrolyte and BE + 4 wt.% LiDFOB d).

developed. Fluorinated solvents or additives are widely used in high-voltage electrolyte formulations due to the unique properties of fluorine, including high oxidative stability, a wide temperature range, and effective interphase formation.[29–31] Representative solvents such as fluoroethylene carbonate (FEC) and methyl (2,2,2-trifluoroethyl) carbonate (FEMC) have been shown to enhance the electrolyte performance of LNMO-based cells.[32,33] However, the incorporation of fluorinated solvents often reduces the solubility of conducting salts and functional additives and increases cost. To address this limitation, fluorinated additives such as tris (2,2,2-trifluoroethyl) phosphate (TTFP) and 1,1,2,2-tetrafluoroethyl 2,2,3,3-tetrafluoropropylether (TTE) have been used in order to optimize the properties of the electrolyte further.[34–36] Despite their functional benefits, there are growing concerns have been mentioned regarding the environmental impact of per- and polyfluoroalkyl substances (PFAS), primarily due to their persistence in the environment. From an environmental standpoint, no —$CF_3$ and —$CF_2$— groups should be present in the conducting salt, solvent/co-solvent, and functional additive(s).[37–39] In this context, the present study aims to develop a PFASfree electrolyte alternative for LNMO||SiGr cells.[40,41] Due to limited options of suitable electrolyte solvents, the elimination of fluorinated solvents makes achieving high voltage stability challenging. An alternative strategy to enhance the high voltage stability is the use of additives improving the CEI function at high voltage.[40,42] Lithium difluoro(oxalato)borate (LiDFOB) is a well-known additive that can suppress electrolyte decomposition, side reactions, and TM dissolution and can effectively enhance overall electrochemical performance.[43–47] Zhang et al. reported that LiDFOB can be employed as a lithium salt due to its solubility in linear carbonates and the ability to reduce the electrolyte viscosity, thereby enhancing the low temperature performance and the rate capability of the $LiNi_{1-x-y}M_xN_yO_2$||Gr cells.[48] More recent studies have identified LiDFOB as a multifunctional additive.

Specifically, it can form effective CEI and SEI layers, suppress electrolyte decomposition, thus enabling improved electrochemical performance of the resulting LNMO||SiGr cell chemistry.[49–51] Ka et al. demonstrated that LiDFOB-based electrolyte formulations, optimized for high-voltage applications, can suppress decomposition and hydrolysis of lithium hexafluorophosphate ($LiPF_6$), capture $Mn^{2+}$ ions, and improve the electrochemical performance of the LNMO||lithium titanium oxide (LTO) cells by forming effective interphases on both the anode (SEI) and cathode (CEI).[49]

In this study, the influence of the electrolyte formulation of 1 m $LiPF_6$ in a mixture of ethylene carbonate (EC) and ethyl methyl carbonate (EMC) (3/7) (BE) in combination with LiDFOB as electrolyte additive for LNMO||SiGr (20 wt.% silicon) cells is investigated. By employing complementary electrochemical and spectroscopic techniques as well as gas chromatography measurements, it is shown that the presence of LiDFOB in an optimum amount of 4 wt.% can considerable improve the galvanostatic cycle life from 145 to 245 cycles (69 %) by suppressing the TM dissolution and scavenging lithium alkoxides.

## 2. Results and Discussion

### 2.1. Galvanostatic Cycling Performance Evaluation

To investigate the role of LiDFOB as an electrolyte additive for LNMO||SiGr cells with a silicon content of 20 wt.% in the SiGr composite, galvanostatic cycling measurements were conducted in a voltage range of 3.5 to 4.9 V. 1 m $LiPF_6$ in EC/EMC (3/7) was used as BE electrolyte and five LiDFOB concentrations ranging from 1 and 5 wt.% were systematically evaluated to determine the optimal formulation for this cell chemistry. **Figure 1** shows the specific discharge capacity vs cycle number during the first 250 cycles a) and accumulated discharge energy until 80 % state of health (SOH) b) of the LNMO||SiGr cells with six considered electrolyte formulations. The cells with the baseline electrolyte show capacity fading during the first 70 cycles, followed by a drastic capacity drop. This results in only 145 cycles until 80 % SOH and an accumulated discharge capacity of 72 Wh $g^{-1}$. Figure 1c displays the difference between the average charge and discharge voltage ($\Delta V$) vs the cycle number. This provides indirect information about the cell polarization, i.e., higher $\Delta V$ values imply a higher cell polarization.[52] For the cells containing the BE electrolyte, a considerably higher cell polarization is observed during the galvanostatic cycling. This indicates faster degradation of the electrodes and the electrolyte decomposition, leading to an increased cell polarization. This observation is consistent with the higher rate of irreversible reactions during long-term cycling, which is indicating by the decreased Coulombic efficiency (CE) values as shown in Figure S1 (Supporting Information).[53] The addition of different amounts of LiDFOB between 1 and 5 wt.% results in a similar galvanostatic cycling performance during the first 140 cycles. The cells with BE + 1 wt.% LiDFOB achieve an improved discharge capacity compared to the BE electrolyte. However, the rapid capacity fading can be postponed by only 30 cycles. This results in an accumulated specific discharge capacity of 88 Wh $g^{-1}$. The $\Delta V$ values are constant for the first 100 cycles, then the $\Delta V$ values increase. The rise in cell polarization can be explained by the rapid capacity fading, which can result from ineffective SEI and CEI formation. A decreased specific discharge capacity is observed with the BE + 2 and 3 wt.% LiDFOB cells compared to the BE + 1 wt.% LiDFOB cells. However, the accumulated discharge capacity improves to 105 and 115 Wh $g^{-1}$respectively. This could be an indication that LiDFOB is continuously consumed during galvanostatic cycling regarding the improved galvanostatic cycling performance with increasing LiDFOB amounts. However, a refill experiment shows that the specific discharge capacity does not increase further if 300 µL of the electrolyte BE + 1 wt.% LiDFOB is added to the aged cell after 178 cycles (Figure S2, Supporting Information). Interestingly, with an increased LiDFOB amount to 4 and 5 wt.% the specific discharge capacity decreases, however, at the same time the capacity fading is postponed to 200 cycles. This results in an improved accumulated specific discharge energy of 120 Wh $g^{-1}$ (BE + 4 wt.% LiDFOB) and of 117 Wh $g^{-1}$ (BE + 5 wt.% LiDFOB). Furthermore, the reduced specific discharge capacity indicates that reduction/oxidation reactions occur at both electrodes during the formation with LiDFOB on the interphases. This is also evident from the decreased CE values, as shown in Figure S1 (Supporting Information). During galvanostatic cycling, the CE is improved, which also demonstrates a beneficial impact of LiDFOB on the interphase formation.[54] LiDFOB concentrations of 4–5 wt. % yield identical cell polarization behavior, indicating suppressed side reactions and the formation of more effective SEI and CEI.

Furthermore, a rate performance investigation was performed to investigate the fast charging capability of the BE and the best performing BE + BE + 4 wt.% LiDFOB electrolyte. Figure 1d shows the comparison of LNMO||SiGr cells containing both electrolyte and shows that the specific discharge capacity is improved for the cells with LiDFOB at all C-rates between 0.1 and 5 C. This means that the developed electrolyte not only improves the cycle life of the LNMO||SiGr cell chemistry, but also enables higher charge and discharge rates.

### 2.2. Capacity Endpoint Slippage Analysis

During galvanostatic cycling of a cell, charge and discharge endpoints progressively shift toward higher capacities. This effect is known as endpoint slippage.[55–57] The shift in the charge endpoint is often attributed to side reactions occurring at the positive electrode, such as electrolyte oxidation, short circuits or shuttling mechanisms.[54–57] In parallel, the discharge endpoint also drifts initially influenced by the charge slippage itself, but may be further affected by parasitic reactions at the negative electrode. The reactions, including the reduction of electrolyte components, results in the loss of active lithium.[55–57] Overall, these slippages serve as a reliable indicator for ongoing parasitic reactions during galvanostatic cycling.[57] **Figure 2a** shows the voltage profiles of the cells with the BE and the best performing BE + 4 wt.% LiDFOB electrolyte. In the cells with BE electrolyte, a more pronounced slippage in both charge and discharge endpoints is observed. The large increase of 0.26 mAh $g^{-1}$ of the discharge endpoints can be related to the particle cracking of the SiGr electrode and the resulting volume change, resulting in an ineffective SEI and severe active lithium loss due to electrolyte decomposition. Furthermore, the observed drop in CE during

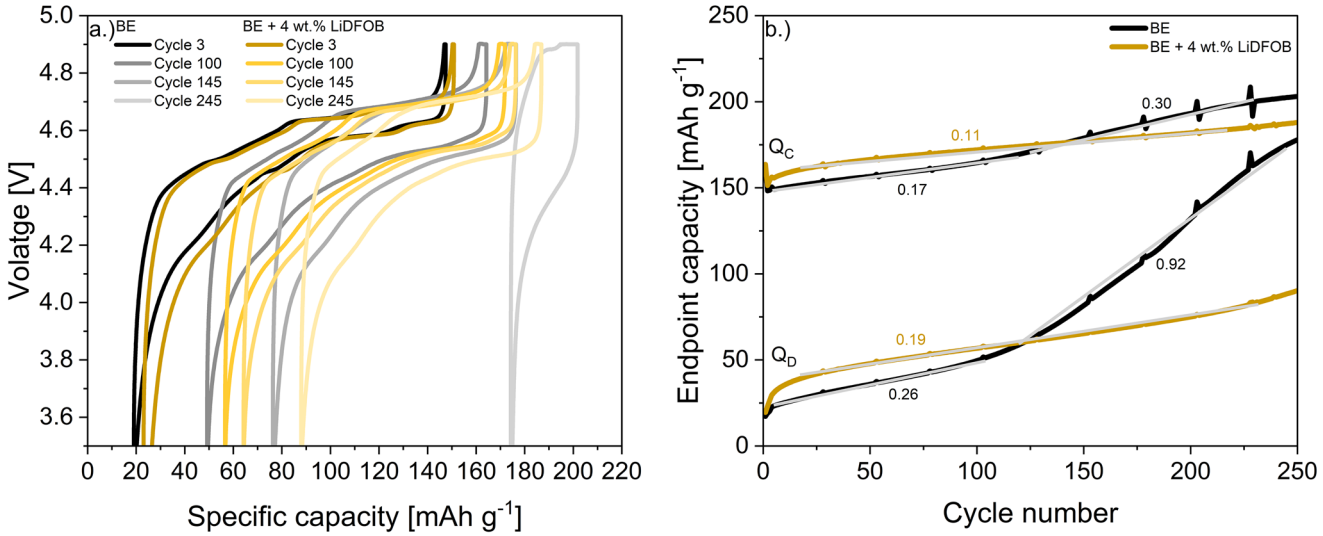


**Figure 2.** Electrochemical charge discharge profile and endpoint capacity vs cycle number of the LNMO||SiGr cells containing BE (black) and BE + 4 wt.% LiDFOB (dark yellow) electrolytes.

galvanostatic cycling further confirms side reactions at the negative electrode.[54,56,57] The capacity endpoint of charge ($Q_C$) exhibits a marching rate of 0.17 mAh $g^{-1}$, suggesting ongoing parasitic oxidation reactions as a result of the formation of ineffective CEI.[54,56] Notably, the charge and discharge endpoint slippage increases drastically after 110 cycles, which can be correlated to the rapid capacity fading and is an indication for irreversible side reactions on both electrodes and ongoing TM dissolution.[54,56,57]

LNMO||SiGr cells containing BE + 4 wt.% LiDFOB electrolyte exhibit a high capacity retention, which aligns with the smaller shifting of voltage profiles (a) and lower slippage during cycling (b), as shown in Figure 2.[55,56] This can be related to the low active lithium loss of the negative electrode and suggests fewer side reactions, indicating the formation of an effective SEI on the SiGr negative electrode due to decomposition products of LiDFOB.[54] Furthermore, $Q_C$ remains nearly constant, which may be attributed to the suppression of side reactions at the positive electrode, likely resulting from the formation of an effective CEI.[32]

### 2.3. Electrolyte Decomposition

To gain a deeper insight into the decomposition products of the BE and BE + 4 wt.% LiDFOB electrolyte, gas chromatography mass spectrometry (GC-MS) measurements were performed of the fresh electrolytes, as well as of the aged electrolytes after 3 cycles and end of life (EOL) (80 % SOH; BE: 145 cycles; BE + 4 wt.% LiDFOB: 245 cycles). **Figure 3** shows the GC-MS analysis of the fresh BE shows prominent peaks, corresponding to EC and EMC solvents. Upon aging, additional signals corresponding to dimethyl carbonate (DMC) and diethyl carbonate (DEC) emerge, indicating ongoing electrolyte decomposition.[58] These changes are attributed to the electrochemical reduction of EC and EMC at the negative electrode, leading to the formation of reactive lithium alkoxides.[59,60] Lithium alkoxides are known to undergo nucleophilic attack on EC and EMC, initiating transesterification reactions,[59,60] resulting in the formation of 2,5-dioxahexane dicarboxylate (EMDOHC), dimethyl 2,5-dioxahexane dicarboxylate (DMDOHC), and diethyl 2,5-dioxahexane dicarboxylate (DEDOHC).[59] Notably, the amount of the transesterification products increased with ongoing cycling. These species have been correlated to parasitic side reactions, resulting in decreased electrochemical performance and increased cell polarization. The addition of 4 wt.% LiDFOB to the BE shows the complete suppression of transesterification products. This suppression is attributed to the effective scavenging of lithium alkoxides by LiDFOB, thereby preventing their participation in transesterification reactions.[47,61] This results in the formation of an effective SEI on the negative electrode surface and inhibits further decomposition of EC and EMC, and reduces side reactions. Consequently, the improved interfacial stability leads to enhanced galvanostatic cycling performance and reduced cell polarization. Furthermore, during the decomposition reactions of $LiPF_6$, highly reactive $PF_5$ is formed, which subsequently leads to the generation of $POF_3$, HF, alkyl fluorides, and carbon dioxide ($CO_2$).[62] During galvanostatic cycling, the decomposition of $LiPF_6$ in the BE + 4 wt.% electrolyte is reduced compared to the BE counterpart.

### 2.4. Gas Evolution During Cell Formation

Gas chromatography barrier discharge ionization detector (GC-BID) and gas chromatography thermal conductivity detector (GC-TCD) measurements were carried out after the formation due to the notable gas development of the cells with the BE + 4 wt.% LiDFOB electrolyte (Figure S3, Supporting Information). In the organic carbonate-based electrolytes, gas evolution during the formation is primarily caused by the reductive instability of EC and EMC within the used voltage range.[63–67] Specifically, the reductive decomposition of EC during the SEI formation generates various gases, including ethene ($C_2H_4$), carbon monoxide (CO), and hydrogen ($H_2$).[63,66,68,69] With the BE electrolyte,

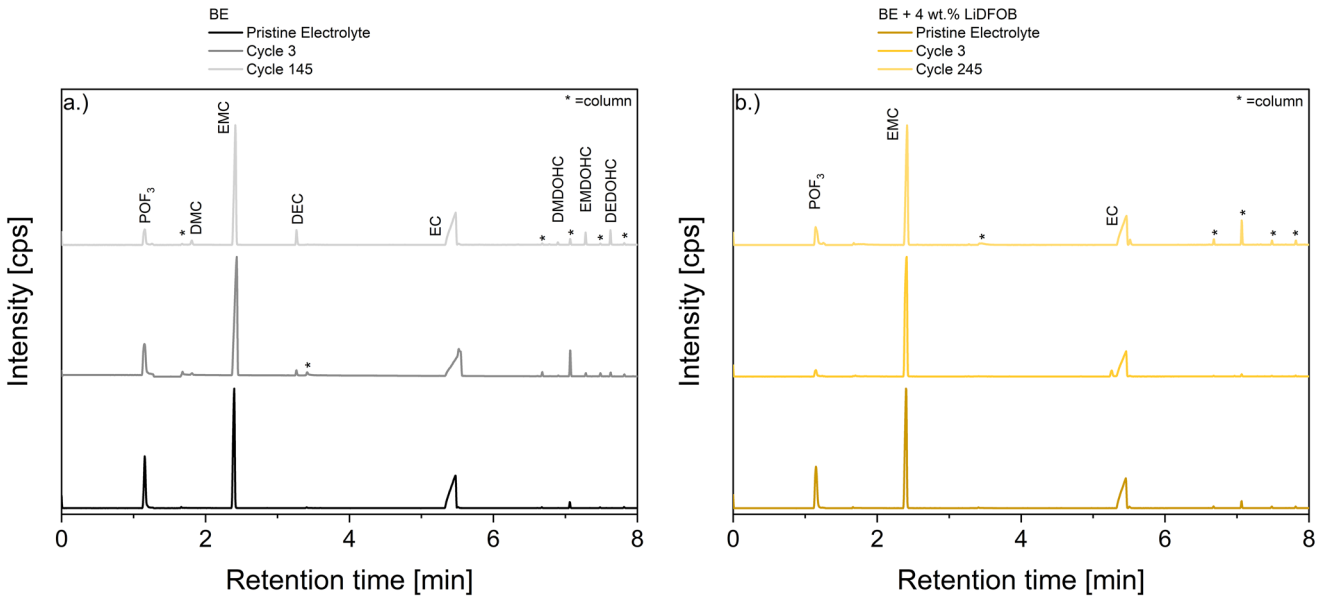


**Figure 3.** GC-MS chromatogram of the fresh and aged BE and BE + 4 wt.% LiDFOB electrolyte.

mainly $H_2$ (52.45 %) is detected as shown in **Figure 4**. $H_2$ is typically produced by the decomposition reaction of trace amounts of $H_2O$ at the negative electrode.[63,66,70,71] Furthermore, the reductive decomposition of the solvent EC leads to the formation of $C_2H_4$ (0.98 %) and $CO_2$ (1.14 %),[72–75] while the decomposition of EMC generates methane ($CH_4$) (1.68 %).[63,73,75] Furthermore, the gas decomposition product ethane ($C_2H_6$) (0.80 %) is also detected.[63,69,72,75] Adding 4 wt.% LiDFOB to the BE leads to a notable gas evolution during the formation, indicating the formation of large quantities of $CO_2$ as the main decomposition product of oxalates.[76] During the oxidative decomposition of LiDFOB, a high amount of $CO_2$ (31.64 %) is formed.[76] $CO_2$ inhibits the formation of lithium alkoxides, which are usually produced by reducing linear carbonates and then undergo transesterification reactions.[76,77]

The $CO_2$ radical produced by anodic reaction also acts as an effective scavenger for $H_2O$ and $H_2$.[76,78] Additionally, the reductive decomposition of EC also produces CO, accounting for another high proportion of the gas composition.[63] According to the literature and linear sweep voltammetry, LiDFOB is reduced before EC (Figure S4, Supporting Information).[79] LiDFOB can suppress both hydrogen formation and the direct reduction of EC, which can limit side reactions with linear carbonates.[79] Due to the preferential reduction of LiDFOB, gaseous products from the reduction of EC or trace impurities (e.g., $CH_4$, $C_2H_6$, $C_2H_4$) only occur in a small fraction.[60] It can be assumed that the decomposition products of LiDFOB enable the formation of a more effective SEI, which suppresses the reduction of solvent components such as EC and reactions with impurities. The remaining gas fraction observed in both samples consists of Ar as well as traces of $O_2$ and $N_2$, introduced during the sample preparation.

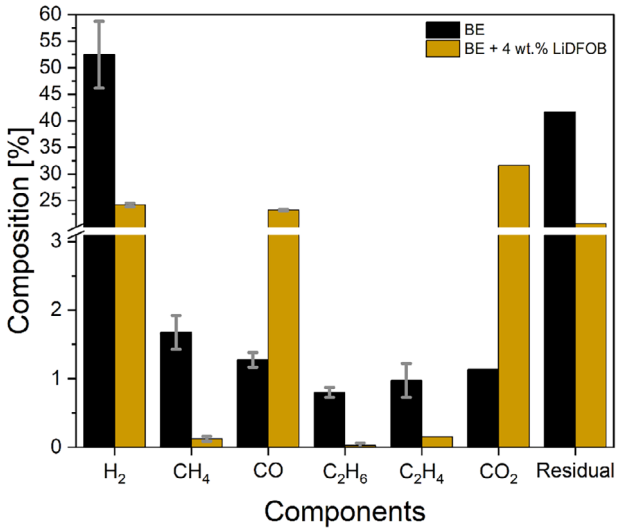


**Figure 4.** GC-BID/TCD measurements of the decomposition products during the formation of the Li-FUN cells containing BE and BE + 4 wt.% LiDFOB electrolytes.

### 2.5. Interphase Characterization

To further investigate the differences in the surface chemistry of the LNMO||SiGr cells containing the BE and BE + 4 wt.% LiDFOB (for simplicity noted as BE + D in the following section) electrolytes, harvested electrodes after 3 cycles and EOL were analyzed using scanning electron microscopy (SEM) and X-ray photoelectron spectroscopy (XPS). While no differences are discernible from the SEM micrographs (Figures S5 and S6, Supporting Information) for either LNMO or SiGr electrodes, the XPS results indicate that both electrolytes have an influence on the SEI and CEI composition. **Figure 5** shows the F 1s spectra of the harvested SiGr electrodes from cells containing BE and BE + D electrolyte. Two peaks are observable, one at ≈685.0 eV, which is attributed to lithium fluoride (LiF), and one at ≈686.5 eV, which is attributed to $Li_xPF_yO_z$.[80,81] In general, LiF and $Li_xPF_yO_z$ are

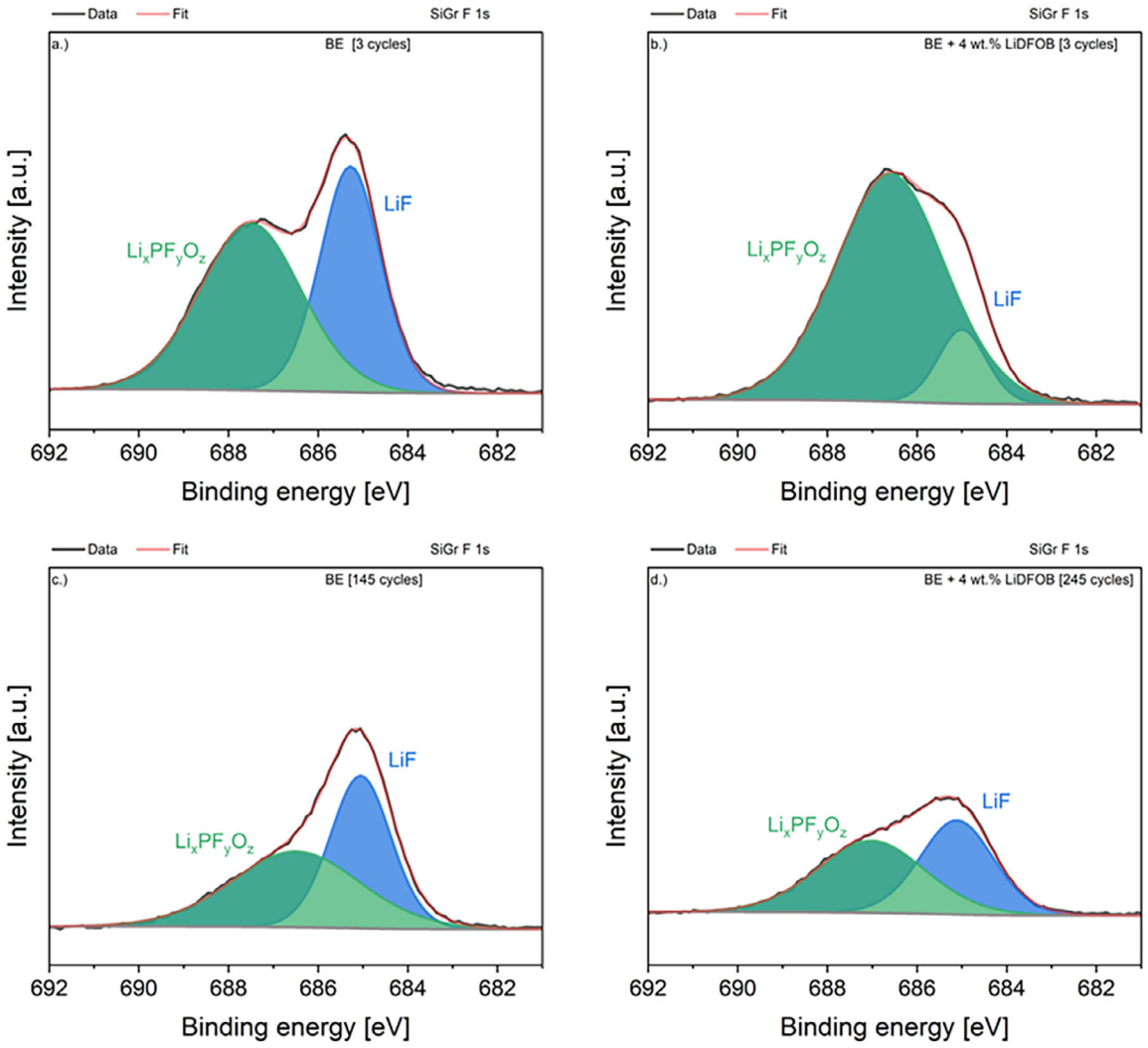


**Figure 5.** F 1s fitting results from XPS spectra of the harvested SiGr electrodes after 3 cycles and after EOL from cells containing considered electrolyte formulations BE (a,c) and BE + 4 wt.% LiDFOB (b,d).

decomposition products of $LiPF_6$, and LiF also being a decomposition product of LiDFOB. After three cycles, considerable differences can be observed with the cells containing different electrolytes. There is a considerably higher relative amount of LiF with the BE electrolyte compared to the cells with the BE + D electrolyte, which could be an indication that in the presence of LiDFOB the fluoride ions are mobilized (e.g. by formation of $BF_4^-$) rather than being deposited in the SEI. As the decomposition of $PF_6^-$ requires the liberation of $F^-$, the detection of fluorophosphates is usually accompanied by a LiF signal of comparable intensity.[82] The LiF amount is increasing for the different electrolytes during galvanostatic cycling, but the LiF amount is still lower for the BE + D electrolyte after EOL. The C 1s spectra of the SiGr electrodes show five peaks, C—C/C=C (graphite) and three characteristic peaks from organic carbonate decomposition products like C—O, O=C—O and $CO_3$ (**Figure 6**).[83] After three cycles and EOL, a higher relative amount of organic decomposition products is observed with the BE + D electrolyte compared to the BE. The proportion of C—O does not change for the BE + D electrolyte during galvanostatic cycling. In contrast, the relative amount of C—O of the BE electrolyte is increasing slightly. This indicates ongoing decomposition reactions of the solvents and conducting salts on the negative electrode. Furthermore, the relative amount of O=C—O and $CO_3$ is increasing during galvanostatic cycling, suggesting that LiDFOB decomposes continuously and more oxalate decomposition products and $Li_2CO_3$ are present in the SEI.[84] These observations are confirmed by the O 1s spectra. (Figure S7, Supporting Information) **Figure 7** shows the presence of the Mn 3p peak in the Li 1s spectra on the SiGr negative electrode with the BE electrolyte after 3 cycles, which shows that manganese has dissolved from the LNMO positive electrode into the electrolyte and subsequently deposited onto the graphite electrode. In contrast, the TM dissolution can be reduced in the presence of the BE + D electrolyte. However, the relative amount of Mn 3p on the negative electrode increases during galvanostatic cycling with both electrolytes. One possible explanation is that, when the LiDFOB is fully consumed during continuous galvanostatic cycling, the TM dissolution of Mn

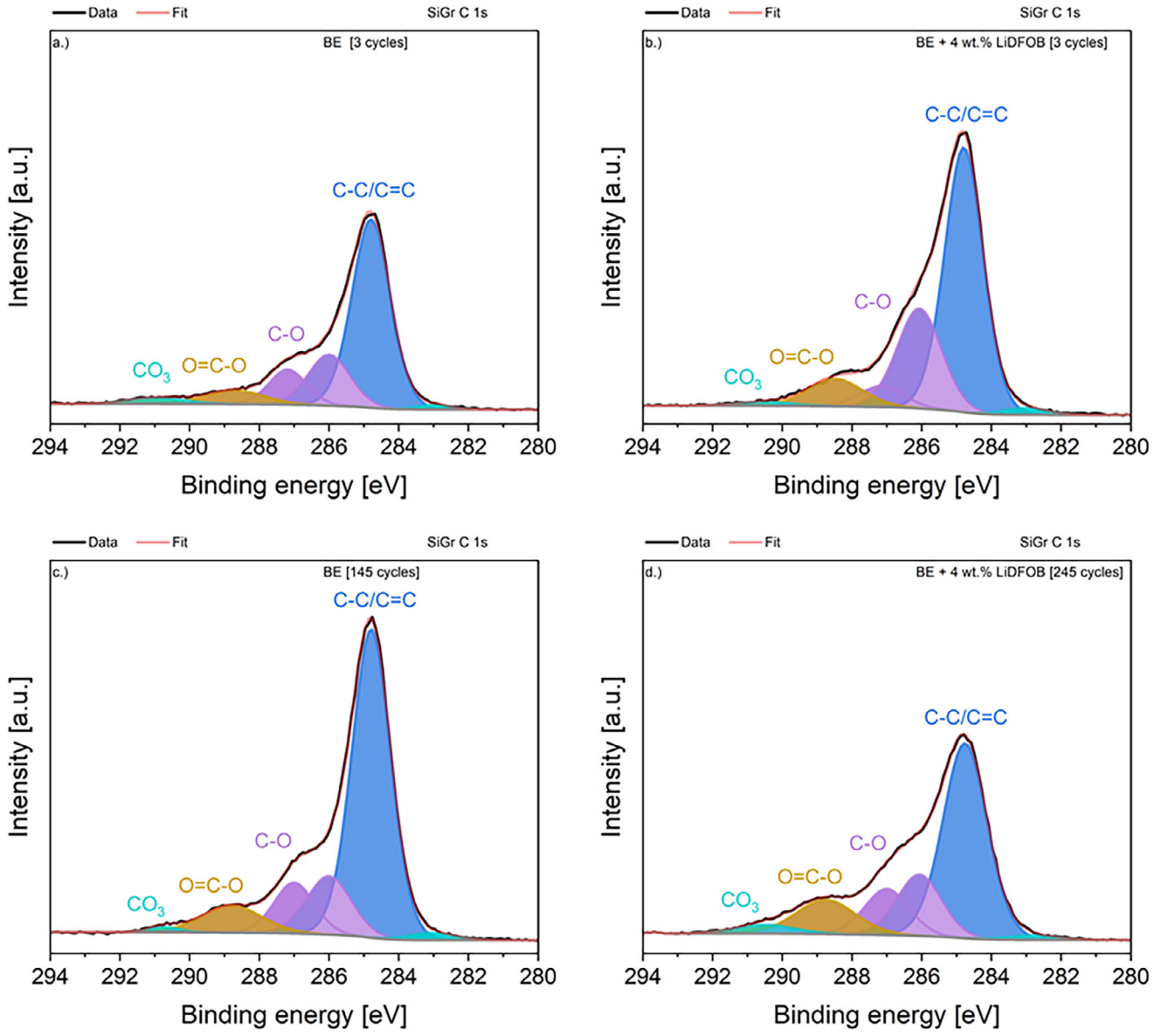


**Figure 6.** C 1s fitting results from XPS spectra of the harvested SiGr electrodes after 3 cycles and after EOL from cells containing considered electrolyte formulations BE (a,c) and BE + 4 wt.% LiDFOB (b,d).

cannot longer be suppressed, resulting in Mn being deposited on the negative electrode. The area of interest in the B 1s spectra overlaps with P 2s signals, which make it impossible to clearly identify contributions by boron. This is especially evident in the BE case, where no boron was present (Figures S8 and S10, Supporting Information).

The XPS measurements on the LNMO positive electrode show small differences between the cells containing BE and the BE + D electrolytes. In the C 1s spectra (**Figure 8**) carbon black and polyvinylidene fluoride (PVDF) $CF_2$ of the binder material can be identified. Additionally, C—C/C=C, C—C, and the classical organic decomposition products like C—O and O=C—O of the electrolyte can be observed.[83] During galvanostatic cycling, the relative amount of the aromatic (C—C/C=C) compounds decreases in the cells with both electrolytes, while the amount of C—C remains unchanged. The relative amount of C—O and O=C—O increases in the cells with both electrolytes during galvanostatic cycling. This indicates an ongoing decomposition of the electrolytes. However, the increase of C—O and O=C—O in the cells with BE + D is stronger, indicating that more oxalate decomposition products are on the CEI.[85] The same trend can be observed in the O 1s spectra (Figure S11, Supporting Information).

## 3. Conclusion

The presence of LiDFOB as a functional additive in an optimal amount of 4 wt.% in the EC/EMC-based electrolyte enhances the cycle life of LNMO||SiGr cells considerably from 145 cycles to 245 cycles (69 %) until 80 % SOH compared to the baseline electrolyte counterpart. The improved performance is attributed

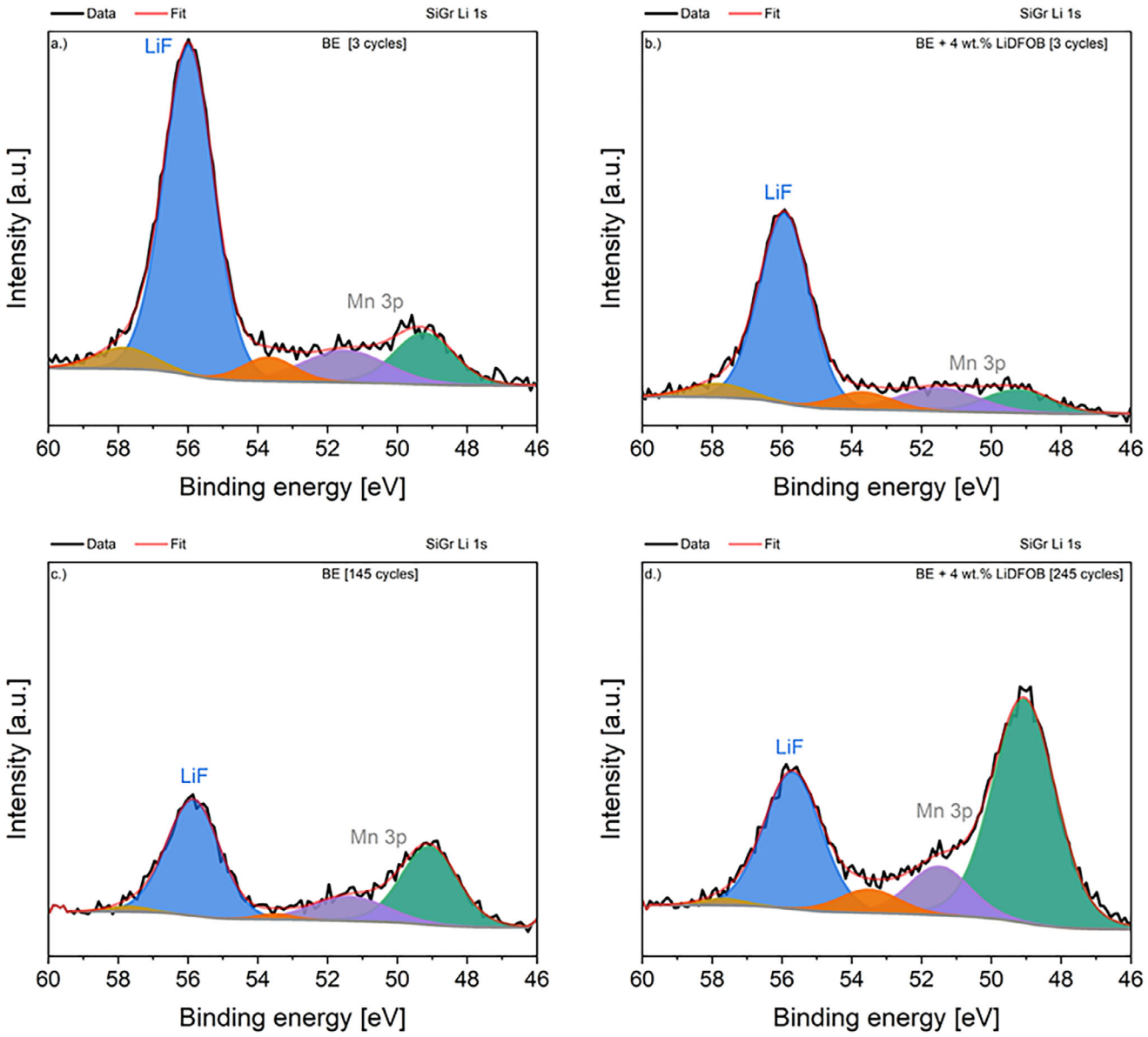


**Figure 7.** Li 1s fitting results from XPS spectra of the harvested SiGr electrodes after 3 cycles and after EOL from cells containing considered electrolyte formulations BE (a,c) and BE + 4 wt.% LiDFOB (b,d).

to several synergistic mechanisms induced by LiDFOB. The incorporation of LiDFOB in the electrolyte is an effective strategy for suppressing side reactions during galvanostatic cycling. Surface analyses of the electrodes show differences in the composition of the SEI and CEI layers between the investigated electrolytes, with a higher abundance of oxalate species detected in the interphase in the presence of LiDFOB. GC measurements have shown that LiDFOB and the gas decomposition product $CO_2$ of LiDFOB can effectively scavenge lithium alkoxides. This also results in a reduction of TM dissolution. Overall, the obtained results underscore the multifunctionality of LiDFOB as a promising PFAS free electrolyte additive that improves the interphase stability and electrochemical performance of the particularly challenging LNMO||SiGr cell chemistry (**Figure 9**).

## 4. Experimental Section

*Electrolyte Components and Resulting Formulations*: Ethyl methyl carbonate (EMC), ethylene carbonate (EC), lithium hexafluorophosphate ($LiPF_6$), and lithium difluoro(oxalato)borate (LiDFOB) were purchased in battery grade quality from E-Lyte innovation GmbH. Electrolytes were formulated per molality (mol $kg^{-1}$) in an argon-filled MBraun glovebox ($H_2O$ <1 ppm, $O_2$ <1 ppm). The following electrolytes were formulated: 1 m $LiPF_6$ in EC/EMC (3/7) and 1 m $LiPF_6$ in EC/EMC (3/7) + X wt.% LiDFOB (X = 1, 2, 3, 4, and 5 wt.%).

*Cell Assembly*: Commercially available 250 mAh LNMO||SiGr (20 % Si) dry two-electrode pouch cells from Li-FUN Technology were used for galvanostatic cycling measurements. The cells were opened and dried under reduced pressure (<0.1 mbar) at 120 °C for 14 h. Following this, the cells were filled with 700 µL of electrolyte and sealed under reduced pressure for 5 s using the pouch cell sealer Gelon GN-HS200V in an

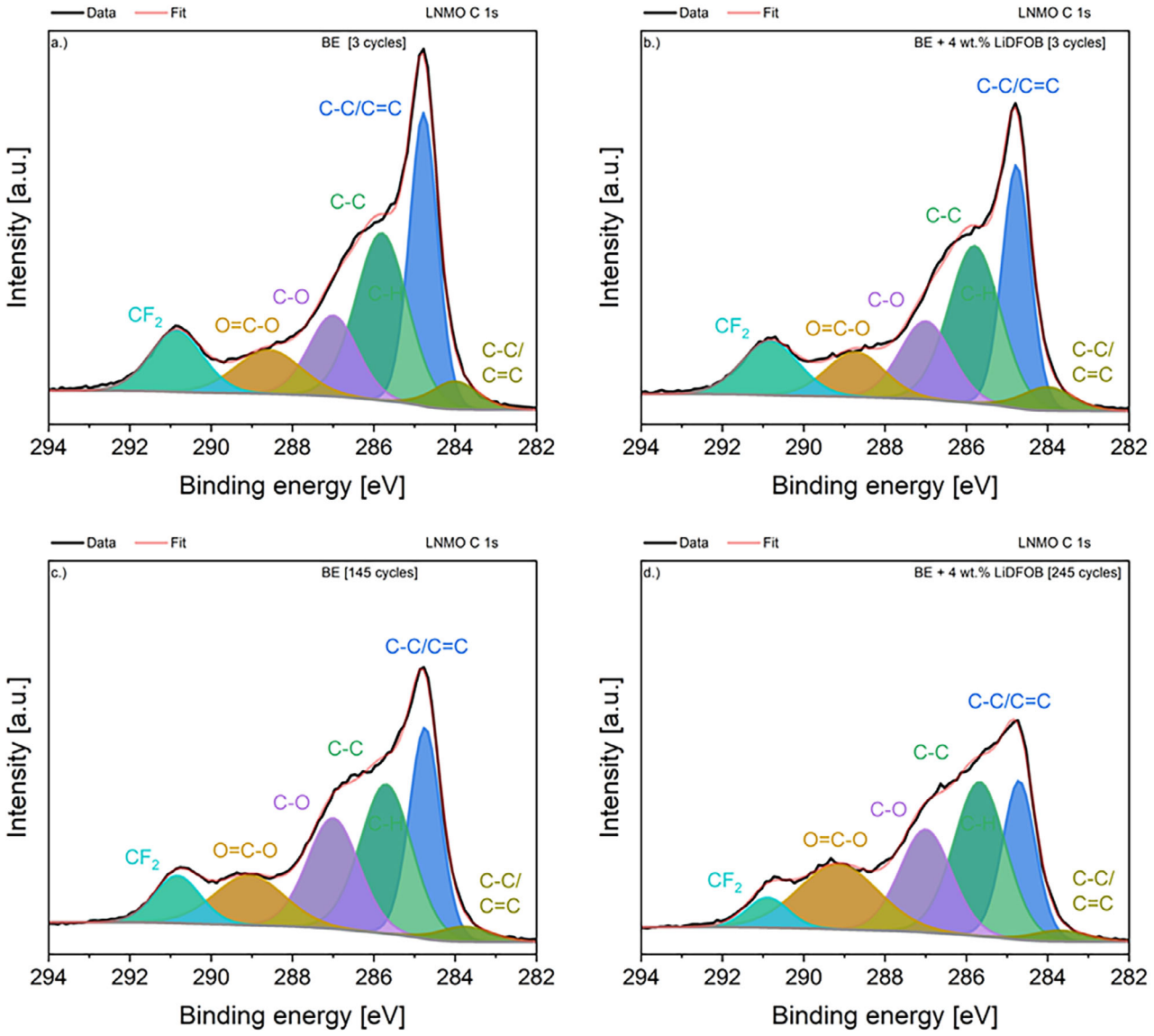


**Figure 8.** C 1s fitting results from XPS spectra of the harvested LNMO electrodes after 3 cycles and after EOL from cells containing considered electrolyte formulations BE (a,c) and BE + 4 wt.% LiDFOB (b,d).

argon-filled MBraun glovebox. ($H_2O$ <1 ppm, $O_2$ <1 ppm) A custom-designed cell holder was employed to ensure a consistent pressure of ≈2 bar was applied using a torque screwdriver. To ensure reproducibility, three cells were assembled for each electrolyte formulation. To prevent excessive gas buildup, cells were cut open in an argon-filled glovebox after the formation cycles and re-sealed using the same procedure as detailed above.

*Electrochemical Performance Evaluation*: Galvanostatic cycling experiments were conducted using a Maccor Series 4000 battery tester in a temperature-controlled chamber at 20 °C. Following a 6 h rest step, three formation cycles were performed at 0.1 C using a constant current/constant voltage (CCCV) protocol within a voltage window of 3.5 to 4.9 V. Subsequent cycling was performed at a C-rate of 0.5 C (CCCV). After every 24 cycles, a capacity check was carried out at 1 C (CCCV).

The rate capability investigations started with a 6 h rest step and then three formation cycles were performed at 0.1 C (CCCV), followed by five cycles at each different C-rate of 0.5, 1.0, 2.0, 3.0, 4.0, 5.0 C (CCCV), and then further galvanostatic cycling at 0.5 C (CCCV).

*Linear Sweep Voltammetry Measurements*: For linear sweep voltammetry, three-electrode EL-Cell PAT cells were used with SiGr as the working electrode, lithium as the counter electrode, and a lithium insulation sleeve with a Freudenberg separator as the reference electrode. A total volume of 100 µL of electrolyte was added to the cell. The measurements were carried out using an MPG-2 Biologic potentiostat/galvanostat at a scan rate of 0.025 mV $s^{-1}$, from open-circuit potential to 0.01 V vs $Li|Li^+$.

*Gas Chromatography–Mass Spectrometry Measurements*: After the 3rd and 100th cycle, the cells were opened inside an argon-filled glovebox. The cell stacks were carefully removed and transferred to centrifugation tubes. The samples were centrifuged at a Sigma 3–18KS at 5500 $min^{-1}$ for 30 min at a temperature of 15 °C. The separated electrolyte was collected and transferred into a GC vial.

GC-MS measurements were conducted using a GC-MS 2030, Shimadzu with a Restek Rxi-5 ms fused silica capillary (30 m, 0.25 mm, 0.25 µm). Volume of 1 µL of the electrolyte sample was injected, with the injector temperature of 200 °C. The initial oven temperature was set to 40 °C, held for 3 min, and followed by a two-step ramp. First, an increase of 12 °C $min^{-1}$

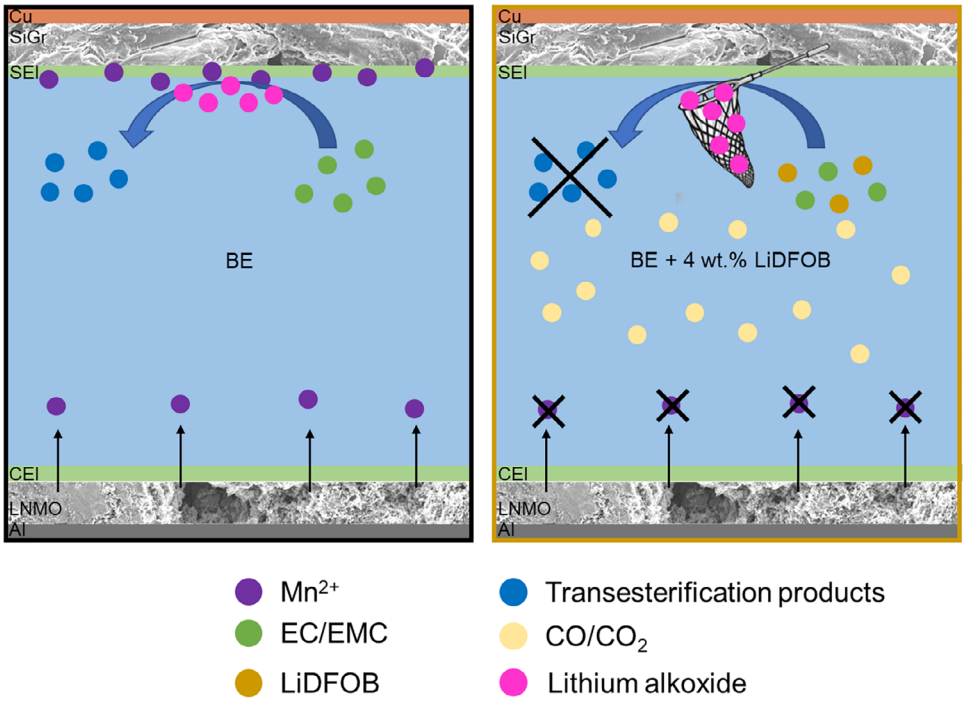


**Figure 9.** Schematic representation of the transesterification process, transesterification products (EMDOHC, DMDOHC, and DEDOHC), and TM dissolution in cells with the BE electrolyte as well as the suppression of the transesterification products formation and the reduction of TM dissolution due to the ability of the LiDFOB-containing electrolyte to scavenge the lithium alkoxide.

to 85 °C and thereafter 33 °C $min^{-1}$ to 210 °C, which leads to a total time of 11 min. The final temperature was held for 2 min. The mass spectrometer was operated in a scan mode over an m/z range of 20–350.

*Gas Chromatography Measurements*: GC measurements were performed using a Shimadzu GC-2010 Plus system with GC parameters and calibration adapted from Leißing et al.[86] For the quantification, a Shimadzu BID BID-2010 Plus and a Shimadzu TCD TCD-2010 Plus detector were used. To control the system, the LabSolutions software (version 5.90) from Shimadzu was used. The gas extraction was adapted by Leißing et al. using a 25 µL gas-tight syringe. The resulting chromatograms were evaluated with the Postrun Analysis editor (version 5.90) from Shimadzu.[86]

*Scanning Electron Microscopy Measurements*: SEM measurements were conducted using a Carl Zeiss AURIGA microscope with an InLens detection mode. The SEM images were acquired with an accelerating voltage of 3 kV and a working distance of 5 mm. Prior to analysis, the electrode samples were prepared by washing them with 1 mL of EMC within an argon-filled glovebox. After washing, the samples were dried and transferred to an air-tight sample chamber.

*X-Ray Photoelectron Spectroscopy Measurements*: XPS measurements were performed using a K-Alpha, Thermo VG Scientific photoelectron spectrometer equipped with a monochromatic Al-K$\alpha$ X-rays (Al K$\alpha$, h$\nu$ = 1486.6 eV). The base pressure of the measuring chamber was $\approx 2 \cdot 10^{-9}$ mbar. Energy calibration was conducted in accordance with ISO 15472 using reference samples of copper, silver, and gold reference. The intensity scale was calibrated following the device manufacturer's specifications. Spectral deconvolution was carried out using a pseudo-Voigt function with 70 % of Gaussian and 30 % of Lorentzian distribution.

## Supporting Information

Supporting Information is available from the Wiley Online Library or from the author.

## Acknowledgements

This project received funding from the European Union's Horizon Europe research and innovation program under grant agreement no. 101069508 (HighSpin).

Open access funding enabled and organized by Projekt DEAL.

## Conflict of Interest

The authors declare no conflict of interest.

## Data Availability Statement

The data that support the findings of this study are available from the corresponding author upon reasonable request.

## Keywords

high silicon content in active material, high voltage application, LiDFOB additive, LNMO electrode, PFAS free electrolyte

Received: September 11, 2025
Revised: October 27, 2025
Published online: November 6, 2025

[1] M. T. Nguyen, H. Q. Pham, J. A. Berrocal, I. Gunkel, U. Steiner, *J. Mater. Chem. A* **2023**, *11*, 7670.
[2] Y. Deng, Z. Li, H. Wang, L. He, B. Zhang, M. Zhang, *Chem. Mater.* **2024**, *36*, 8037.

[3] R. Azmi, F. Lindgren, K. Stokes-Rodriguez, M. Buga, C. Ungureanu, T. Gouveia, I. Christensen, S. Pal, A. Vlad, A. Ladam, K. Edström, M. Hahlin, *ACS Appl. Mater. Interfaces* **2024**, *16*, 34266.
[4] G. G. Eshetu, H. Zhang, X. Judez, H. Adenusi, M. Armand, S. Passerini, E. Figgemeier, *Nat. Commun.* **2021**, *12*, 5459.
[5] G. Liang, V. K. Peterson, K. W. See, Z. Guo, W. K. Pang, *J. Mater. Chem. A* **2020**, *8*, 15373.
[6] C. Wölke, B. A. Sadeghi, G. G. Eshetu, E. Figgemeier, M. Winter, I. Cekic-Laskovic, *Adv. Mater. Interfaces* **2022**, *9*, 2101898.
[7] Y. Jin, B. Zhu, Z. Lu, N. Liu, J. Zhu, *Adv. Energy Mater.* **2017**, *7*, 1700715.
[8] M. N. Obrovac, L. Christensen, *Electrochem. Solid-State Lett.* **2004**, *7*, A93.
[9] M. T. McDowell, S. W. Lee, W. D. Nix, Y. Cui, *Adv. Mater.* **2013**, *25*, 4966.
[10] C. Chae, H. Noh, J. K. Lee, B. Scrosati, Y. Sun, *Adv. Funct. Mater.* **2014**, *24*, 3036.
[11] K. Feng, M. Li, W. Liu, A. G. Kashkooli, X. Xiao, M. Cai, Z. Chen, *Small* **2018**, *14*, 1702737.
[12] M. Gautam, G. K. Mishra, K. Bhawana, C. S. Kalwar, D. Dwivedi, A. Yadav, S. Mitra, *ACS Appl. Mater. Interfaces* **2024**, *16*, 45809.
[13] U. Kasavajjula, C. Wang, A. J. Appleby, *J. Power Sources* **2007**, *163*, 1003.
[14] Z. Yang, S. E. Trask, X. Wu, B. J. Ingram, *Batteries* **2023**, *9*, 138.
[15] Z. Yan, S. Yi, X. Li, J. Jiang, D. Yang, N. Du, *Mater. Today Energy* **2023**, *31*, 101225.
[16] R. Zhao, L. Li, T. Xu, D. Wang, D. Pan, G. He, H. Zhao, Y. Bai, *ACS Appl. Mater. Interfaces* **2019**, *11*, 16233.
[17] Z. Zou, H. Xu, H. Zhang, Y. Tang, G. Cui, *ACS Appl. Mater. Interfaces* **2020**, *12*, 21368.
[18] L. Chladil, D. Kunický, T. Kazda, P. Vanýsek, O. Čech, P. Bača, *J. Energy Storage* **2021**, *41*, 102907.
[19] J. Mu, X. Li, R. He, L. Sun, X. Bai, L. Zhang, P. Liu, Z. Liu, J. Gao, A. Wei, *J. Energy Storage* **2024**, *96*, 112538.
[20] T. Horiba, *Proc. IEEE* **2014**, *102*, 939.
[21] Y. Huang, Y. Dong, S. Li, J. Lee, C. Wang, Z. Zhu, W. Xue, Y. Li, J. Li, *Adv. Energy Mater.* **2021**, *11*, 2000997.
[22] Y. Hao, Q. Yang, R. Gao, Y. Saixi, Z. Chen, W. He, H. Zhao, *Int. J. Electrochem. Sci.* **2025**, *20*, 101002.
[23] T. Fu, D. Lu, Z. Yao, Y. Li, C. Luo, T. Yang, S. Liu, Y. Chen, Q. Guo, C. Zheng, W. Sun, *J. Mater. Chem. A* **2023**, *11*, 13889.
[24] R. Santhanam, B. Rambabu, *J. Power Sources* **2010**, *195*, 5442.
[25] M.-C. Kim, Y.-W. Lee, T. K. Pham, J. I. Sohn, K.-W. Park, *Appl. Surf. Sci.* **2020**, *504*, 144514.
[26] D. Zhou, F. Lin, J. Song, J. Guo, *J. Mater. Sci.: Mater. Electron.* **2022**, *33*, 16621.
[27] W. Huang, L. Yan, L. Zhang, X. Zhang, Z. Wu, C. Zhu, Z. Fang, K. Yang, *Electrochim. Acta* **2023**, *458*, 142525.
[28] Z. Zhang, C. Chang, J. Zheng, *J. Energy Storage* **2024**, *99*, 113226.
[29] Y. Wang, X. Yang, Y. Meng, Z. Wen, R. Han, X. Hu, B. Sun, F. Kang, B. Li, D. Zhou, C. Wang, G. Wang, *Chem. Rev.* **2024**, *124*, 3494.
[30] Z. Pan, H. Chen, Y. Zeng, Y. Ding, X. Pu, Z. Chen, *Energy Mater.* **2023**, *3*, 300054.
[31] Y. Wang, Z. Li, Y. Hou, Z. Hao, Q. Zhang, Y. Ni, Y. Lu, Z. Yan, K. Zhang, Q. Zhao, F. Li, J. Chen, *Chem. Soc. Rev.* **2023**, *52*, 2713.
[32] M. Leopold, F. Pfeiffer, E. C. Muschiol, C. Wölke, P. Yan, K. Brüning, S. Nowak, M. Esselen, M. Winter, I. Cekic-Laskovic, *Small* **2025**, *21*, 2505254.
[33] W. Yao, Y. Li, M. Olguin, S. Bai, M. A. Schroeder, W. Li, A. Liu, N. R. Park, B. Bhamwala, B. Sayahpour, G. Raghavendran, O. Borodin, M. Zhang, Y. S. Meng, *Next Energy* **2024**, *4*, 100136.
[34] R. I. Pushparaj, A. R. Kumar, G. Xu, *J. Energy Storage* **2023**, *72*, 108493.
[35] Y. Gu, S. Fang, L. Yang, S. Hirano, *ACS Appl. Energy Mater.* **2021**, *4*, 4919.
[36] L. Xia, M. Chen, F. Wang, H. Miao, J. Yuan, *J. Power Sources* **2022**, *526*, 231152.
[37] A. Rensmo, E. K. Savvidou, I. T. Cousins, X. Hu, S. Schellenberger, J. P. Benskin, *Environ. Sci.: Processes Impacts* **2023**, *25*, 1015.
[38] C. Schiavone, C. Portesi, *Appl. Sci.* **2023**, *13*, 6696.
[39] T. Mohr, I. Schliebner, M. Neumann, L. Oules, H. P. H. Arp, S. E. Hale, *Environ. Sci. Eur.* **2024**, *36*, 99.
[40] X. Fan, C. Wang, *Chem. Soc. Rev.* **2021**, *50*, 10486.
[41] K.-C. Möller, T. Hodal, W. K. Appel, M. Winter, J. O. Besenhard, *J. Power Sources* **2001**, *97–98*, 595.
[42] W. Zhao, Y. Ji, Z. Zhang, M. Lin, Z. Wu, X. Zheng, Q. Li, Y. Yang, *Curr. Opin. Electrochem.* **2017**, *6*, 84.
[43] S. S. Zhang, *J. Power Sources* **2007**, *163*, 713.
[44] D. P. Abraham, M. M. Furczon, S.-H. Kang, D. W. Dees, A. N. Jansen, *J. Power Sources* **2008**, *180*, 612.
[45] A. Jamal, G. D. Salian, A. Mathew, W. Wahyudi, R. P. Carvalho, R. Gond, S. K. Heiskanen, D. Brandell, R. Younesi, *ChemElectroChem* **2023**, *10*, 202300139.
[46] B. Wang, S.-B. Son, P. Badami, S. E. Trask, D. Abraham, Y. Qin, Z. Yang, X. Wu, A. Jansen, C. Liao, *Batteries* **2023**, *9*, 435.
[47] B. Wang, J. C. Garcia, J. Chen, S.-B. Son, S. E. Trask, Y. Qin, H. H. Iddir, C. Liao, *ACS Appl. Eng. Mater.* **2024**, *2*, 2910.
[48] S. S. Zhang, *Electrochem. Commun.* **2006**, *8*, 1423.
[49] O. Ka, F. Cheng, L. Wen, X. Wang, T. Wang, X. Zeng, W. Lu, L. Dai, *J. Mater. Chem. A* **2024**, *12*, 11487.
[50] L. Zhang, X. Dong, H. Lin, X. Zhang, Y. Wang, C. Wang, H.-M. Ye, T. Cao, G. Huang, *J. Mater. Sci.: Mater. Electron.* **2024**, *35*, 524.
[51] J. Liu, Z. Chen, S. Busking, K. Amine, *Electrochem. Commun.* **2007**, *9*, 475.
[52] A. Gomez-Martin, F. Reissig, L. Frankenstein, M. Heidbüchel, M. Winter, T. Placke, R. Schmuch, *Adv. Energy Mater.* **2022**, *12*, 2103045.
[53] M. Weiling, F. Pfeiffer, C. Lechtenfeld, S. Stuckenberg, N. Fehlings, L. Frankenstein, V. Küpers, J. Wang, S. Nowak, M. Baghernejad, *Batteries Supercaps* **2025**, *8*, 202400568.
[54] P. Yan, M. Shevchuk, C. Wölke, F. Pfeiffer, D. Berghus, M. Baghernejad, G. Röschenthaler, M. Winter, I. Cekic-Laskovic, *Small Struct.* **2024**, *5*, 2300425.
[55] A. J. Smith, J. C. Burns, D. Xiong, J. R. Dahn, *J. Electrochem. Soc.* **2011**, *158*, A1136.
[56] V. Meunier, M. Leal De Souza, M. Morcrette, A. Grimaud, *Joule* **2023**, *7*, 42.
[57] A. Arifiadi, L. Wichmann, T. Brake, C. Lechtenfeld, J. Buchmann, F. Demelash, P. Yan, G. Brunklaus, I. Cekic-Laskovic, S. Wiemers-Meyer, M. Winter, J. Kasnatscheew, *Small* **2025**, *21*, 2410762.
[58] F. Pfeiffer, A. Griggio, M. Weiling, J. Wang, F. Reißig, C. Peschel, L. Pillatsch, S. Warrington, S. Nowak, V. Grimaudo, I. Wright, M. Baghernejad, *Adv. Energy Mater.* **2024**, *14*, 2402187.
[59] F. Demelash, A. Arifiadi, B. Heidrich, E. Adhitama, C.-T. Lechtenfeld, N. M. Abke, M. Weiling, J. F. Wang, D. Diddens, S. Wiemers-Meyer, M. Winter, M. Baghernejad, P. Niehoff, *Energy Storage Mater.* **2024**, *72*, 103735.
[60] A. Ghaur, C. Peschel, I. Dienwiebel, L. Haneke, L. Du, L. Profanter, A. Gomez-Martin, M. Winter, S. Nowak, T. Placke, *Adv. Energy Mater.* **2023**, *13*, 2370113.
[61] Y. Zhu, Y. Li, M. Bettge, D. P. Abraham, *J. Electrochem. Soc.* **2012**, *159*, A2109.
[62] V. Kraft, W. Weber, B. Streipert, R. Wagner, C. Schultz, M. Winter, S. Nowak, *RSC Adv.* **2016**, *6*, 8.
[63] J.-P. Schmiegel, M. Leißing, F. Weddeling, F. Horsthemke, J. Reiter, Q. Fan, S. Nowak, M. Winter, T. Placke, *J. Electrochem. Soc.* **2020**, *167*, 060516.
[64] B. B. Berkes, A. Schiele, H. Sommer, T. Brezesinski, J. Janek, *J. Solid State Electrochem.* **2016**, *20*, 2961.

[65] L. D. Ellis, J. P. Allen, L. M. Thompson, J. E. Harlow, W. J. Stone, I. G. Hill, J. R. Dahn, *J. Electrochem. Soc.* **2017**, *164*, A3518.
[66] R. Bernhard, M. Metzger, H. A. Gasteiger, *J. Electrochem. Soc.* **2015**, *162*, A1984.
[67] R. Jung, M. Metzger, D. Haering, S. Solchenbach, C. Marino, N. Tsiouvaras, C. Stinner, H. A. Gasteiger, *J. Electrochem. Soc.* **2016**, *163*, A1705.
[68] R. Nölle, J.-P. Schmiegel, M. Winter, T. Placke, *Chem. Mater.* **2020**, *32*, 173.
[69] H. Ota, Y. Sakata, A. Inoue, S. Yamaguchi, *J. Electrochem. Soc.* **2004**, *151*, A1659.
[70] M. Metzger, B. Strehle, S. Solchenbach, H. A. Gasteiger, *J. Electrochem. Soc.* **2016**, *163*, A798.
[71] R. Imhof, P. Novák, *J. Electrochem. Soc.* **1998**, *145*, 1081.
[72] M. Onuki, S. Kinoshita, Y. Sakata, M. Yanagidate, Y. Otake, M. Ue, M. Deguchi, *J. Electrochem. Soc.* **2008**, *155*, A794.
[73] X. Teng, C. Zhan, Y. Bai, L. Ma, Q. Liu, C. Wu, F. Wu, Y. Yang, J. Lu, K. Amine, *ACS Appl. Mater. Interfaces* **2015**, *7*, 22751.
[74] R. Mogi, M. Inaba, Y. Iriyama, T. Abe, Z. Ogumi, *J. Power Sources* **2003**, *119*, 597.
[75] J.-S. Shin, C.-H. Han, U.-H. Jung, S.-I. Lee, H.-J. Kim, K. Kim, *J. Power Sources* **2002**, *109*, 47.
[76] S. Solchenbach, M. Wetjen, D. Pritzl, K. U. Schwenke, H. A. Gasteiger, *J. Electrochem. Soc.* **2018**, *165*, A512.
[77] B. Strehle, S. Solchenbach, M. Metzger, K. U. Schwenke, H. A. Gasteiger, *J. Electrochem. Soc.* **2017**, *164*, A2513.
[78] K. U. Schwenke, S. Solchenbach, J. Demeaux, B. L. Lucht, H. A. Gasteiger, *J. Electrochem. Soc.* **2019**, *166*, A2035.
[79] T. Melin, R. Lundström, E. J. Berg, *J. Phys. Chem. Lett.* **2024**, *15*, 2537.
[80] M. He, C.-C. Su, C. Peebles, Z. Feng, J. G. Connell, C. Liao, Y. Wang, I. A. Shkrob, Z. Zhang, *ACS Appl. Mater. Interfaces* **2016**, *8*, 11450.
[81] T. Eriksson, A. M. Andersson, C. Gejke, T. Gustafsson, J. O. Thomas, *Langmuir* **2002**, *18*, 3609.
[82] J. Han, K. Kim, Y. Lee, N. Choi, *Adv. Mater.* **2019**, *31*, 1804822.
[83] D. Martín-Yerga, D. C. Milan, X. Xu, J. Fernández-Vidal, L. Whalley, A. J. Cowan, L. J. Hardwick, P. R. Unwin, *Angew. Chem. Int. Ed.* **2022**, *61*, 202207184.
[84] C.-Y. Liu, Y. Yang, M. Yao, H.-T. Fang, *Energy Storage Mater.* **2019**, *18*, 148.
[85] M. Xu, L. Zhou, L. Hao, L. Xing, W. Li, B. L. Lucht, *J. Power Sources* **2011**, *196*, 6794.
[86] M. Leißing, M. Winter, S. Wiemers-Meyer, S. Nowak, *J. Chromatogr. A* **2020**, *1622*, 461122.